Geomorphology 109 (2009) 132–147

Contents lists available at ScienceDirect

Geomorphology

journal homepage: www.elsevier.com/locate/geomorph

Automated landslide mapping using spectral analysis and high-resolution topographic data: Puget Sound lowlands, Washington, and Portland Hills, Oregon

Adam M. Booth [a,*], Josh J. Roering [a], J. Taylor Perron [b,1]

[a] University of Oregon, Department of Geological Sciences, 1272 University of Oregon, Eugene, OR 97403-1272, USA
[b] Harvard University, Department of Earth & Planetary Sciences, 20 Oxford St., Cambridge, MA 02138, USA

ARTICLE INFO

Article history:
Received 4 November 2008
Received in revised form 23 February 2009
Accepted 25 February 2009
Available online 10 March 2009

Keywords:
Fourier
Landslide map
LiDAR
Tualatin
Puget
Wavelet

ABSTRACT

Landslide inventory maps are necessary for assessing landslide hazards and addressing the role slope stability plays in landscape evolution over geologic timescales. However, landslide inventory maps produced with traditional methods — aerial photograph interpretation, topographic map analysis, and field inspection — are often subjective and incomplete. The increasing availability of high-resolution topographic data acquired via airborne Light Detection and Ranging (LiDAR) over broad swaths of terrain invites new, automated landslide mapping procedures. We present two methods of spectral analysis that utilize LiDAR-derived digital elevation models of the Puget Sound lowlands, Washington, and the Tualatin Mountains, Oregon, to quantify and automatically map the topographic signatures of deep-seated landslides. Power spectra produced using the two-dimensional discrete Fourier transform and the two-dimensional continuous wavelet transform identify the characteristic spatial frequencies of deep-seated landslide morphologic features such as hummocky topography, scarps, and displaced blocks of material. Spatial patterns in the amount of spectral power concentrated in these characteristic frequency bands highlight past slope instabilities and allow the delineation of landslide terrain. When calibrated by comparison with detailed, independently compiled landslide inventory maps, our algorithms correctly classify an average of 82% of the terrain in our five study areas. Spectral analysis also allows the creation of dominant wavelength maps, which prove useful in analyzing meter-scale topographic expressions of landslide mechanics, past landslide activity, and landslide-modifying geomorphic processes. These results suggest that our automated landslide mapping methods can create accurate landslide maps and serve as effective, objective, and efficient tools for digital terrain analysis.

© 2009 Elsevier B.V. All rights reserved.

1. Introduction

Creating detailed landslide inventory maps is a first step in assessing landslide hazards for policy-making purposes (Wieczorek, 1984), as well as in answering scientific questions involving spatial and temporal patterns of mass movement. Traditional landslide mapping methods include scanning topographic maps for opposing and irregular contours, interpreting aerial photographs using a stereoscope, and directly observing landslide morphology in the field (Nilsen and Brabb, 1977; Nilsen et al., 1979; Cruden and Varnes, 1996; Guzzetti et al., 1999; Wills and McCrink, 2002; Galli et al., 2008). However, each of these methods has limitations that may reduce the scope and accuracy of the resulting landslide map (Malamud et al., 2004a; Roering et al., 2005). Topographic maps often lack the resolution required to map small or topographically subtle landslides, while vegetation often obscures morphologic features indicative of landslides in aerial photographs. Detailed field mapping is time intensive and difficult to carry out in rugged, forested terrain (Van Den Eeckhaut et al., 2005). Furthermore, landslides located using any method must be translated to a paper or digital map, which introduces additional errors (Malamud et al., 2004a). For these reasons, landslide inventories prepared by traditional means are often incomplete (Malamud et al., 2004b), and maps of a given area produced by different workers often differ dramatically (Guzzetti et al., 2000; Wills and McCrink, 2002; Galli et al., 2008). Use of incomplete or uncertain landslide inventories has clear implications for hazard assessment and may also skew the landslide distribution statistics used to estimate sediment production and transport (Hovius et al., 2000; Malamud et al., 2004a).

The increasing availability of high-resolution digital elevation models (DEMs) derived from airborne Light Detection and Ranging (LiDAR) measurements provides an additional tool for analyzing the geomorphic expression of deep-seated landslides over broad swaths of terrain. Airborne LiDAR can pierce vegetative cover and, with processing, reveal sub meter-scale features of the ground surface in many regions (Slatton et al., 2007). Many recent mapping efforts have taken advantage of LiDAR-derived DEMs to map landslides in forested terrain with improved results compared to traditional methods

* Corresponding author. Tel.: +1 541 346 4354; fax: +1 541 346 4692.
E-mail address: abooth@uoregon.edu (A.M. Booth).
[1] Now at Massachusetts Institute of Technology, Department of Earth, Atmospheric, and Planetary Sciences, 77 Massachusetts Ave., Cambridge, MA 02139, USA.

0169-555X/$ – see front matter © 2009 Elsevier B.V. All rights reserved.
doi:10.1016/j.geomorph.2009.02.027

(Haugerud et al., 2003; Schulz, 2004, 2005, 2007; Van Den Eeckhaut et al., 2007a). Still, experts often disagree about which topographic features indicate landslides in a given LiDAR data set, and landslide mapping remains somewhat subjective (Guzzetti et al., 2000; Van Den Eeckhaut et al., 2005, 2007a).

An advantage of the high resolution of LiDAR-derived DEMs is that it allows more objective and quantitative analysis of fine-scale land surface features associated with a host of geomorphic processes, including landsliding. Several recent studies have illustrated how visual and statistical analyses of landslide topography can highlight patterns of surface deformation at specific sites (McKean and Roering, 2004; Chadwick et al., 2005; Glenn et al., 2006; Van Den Eeckhaut et al., 2007b). However, few studies have utilized large, high-resolution data sets to quantitatively investigate broad spatial patterns of landsliding (Hovius et al., 1997; Roering et al., 2005).

Here, we aim to develop new methodologies that utilize the Fourier and continuous wavelet transforms to automatically extract the topographic signatures of past deep-seated landslides from high-resolution topographic data. Specifically, variations in spectral power within spatial frequency bands characteristic of deep-seated landslides allow us to efficiently produce accurate kilometer-scale, deep-seated landslide maps. We also generate dominant wavelength maps and demonstrate their effectiveness in analyzing meter-scale topographic expressions of landslide mechanics, past landslide activity, and landslide-modifying geomorphic processes such as soil creep.

2. Study areas

We selected two main study areas — the Tualatin Mountains, Oregon, and the Puget Sound lowlands, Washington — based on the availability of high-resolution, LiDAR-derived DEMs and detailed, independently compiled landslide inventory maps. Figs. 1–3 show LiDAR-derived hillshade maps of the study areas, which we divide into five smaller sections for analysis: the Dixie Mountain quadrangle (DMQ) and northwest Dixie Mountain quadrangle (NWD), Oregon (Fig. 1), marine Thurston County (MTC) and the Carlyon Beach Peninsula (CBP), Washington (Fig. 2), and Seattle (SEA), Washington (Fig. 3). Although the independently compiled inventory maps represent workers' interpretations of landslide features and are therefore not completely objective, they are the most current maps of our study areas and provide an outside standard with which we compare our algorithm performance. Portions of the study areas contain debris flow deposits and shallow landslides, but we focus specifically on the morphologic signatures of deep-seated landslide processes in this study.

2.1. Tualatin Mountains, Oregon

The Dixie Mountain quadrangle contains the NW–SE trending Tualatin Mountains, which drop 300 m or more in elevation to the Columbia River floodplain in the northeastern part of the quadrangle. Bedrock consists primarily of deeply weathered Columbia River flood basalts, which unconformably overlie weathered marine sandstone and siltstone of the Scappoose Formation (Trimble, 1963). An ~10–30 m blanket of loess accumulated during the late Pleistocene and is preserved on many of the high, low-angle ridges (Trimble, 1963; Madin and Niewendorp, 2008). This loess-mantled surface appears smooth in the LiDAR-derived hillshade map and is especially well preserved along the spine of the Tualatin Mountains (along the SW edge of Fig. 1). Large landslide complexes occupy most of the northeastern slopes of the Tualatin Mountains where rivers have cut through the basalt and exposed the underlying Scappoose Formation (Trimble, 1963). Primary failure planes of the landslide complexes typically occur in weak layers of the Scappoose Formation at least tens of meters below the present surface (Madin and Niewendorp, 2008). In the LiDAR-derived hillshade map (Fig. 1), surfaces of these deep-seated landslides appear rough with many scarps, blocks undergoing tensile failure, and flow-like features clearly visible.

We acquired a LiDAR-derived DEM with 3-ft (0.9-m) point spacing of the Dixie Mountain quadrangle from the Oregon LiDAR Consortium (http://www.oregongeology.com/sub/projects/olc/). Madin and Niewendorp (2008) used field observations and interpretation of geomorphic features on a LiDAR-derived DEM to produce both a bedrock map and a surface deposit map of the quadrangle. LiDAR-derived DEMs were not available for previous mapping of the surrounding areas (Beeson et al., 1989, 1991), and previous maps included only bedrock units or a mix of bedrock units and surface deposits. In their surface map, Madin and Niewendorp (2008) classify landslide deposits based on style, age, and composition into five units: flow and fan deposits, surficial landslides, bedrock landslides, the Wildwood landslide complex, and the Dutch Canyon landslide complex. In our analysis of the DMQ and NWD study areas (Fig. 1), we use only deep-seated landslide units including bedrock landslides and the Wildwood and Dutch Canyon landslide complexes, which cover 53% of DMQ and 80% of NWD.

2.2. Puget Sound lowlands, Washington

The stratigraphy and surface morphology of most of the southern Puget Sound lowlands reflect the most recent interglacial–glacial cycle (Tubbs, 1974, 1975; Galster and Laprade, 1991; Haugerud et al., 2003). Nonglacial clay, silt, and sand deposited during the Olympia interglacial underlie glacial sediments of the Vashon stade of the Fraser glaciation (Armstrong et al., 1965; Booth, 1987). These loosely consolidated sediments are commonly exposed in 50-m or higher bluffs that truncate a glacially sculpted upland surface (Galster and Laprade, 1991; Schulz, 2004, 2007). In the LiDAR-derived hillshade maps (Figs. 2 and 3), this upland surface appears broadly undulating with many elongate, N–S trending drumlins. Following glaciation, isostatic rebound elevated the glacially sculpted surface while eustatic sea level and lake levels rose (Booth, 1987), undercutting adjacent slopes (Tubbs, 1974, 1975; Schulz, 2004, 2005, 2007). Coastal erosion, accomplished largely by deep-seated landsliding, resulted. Topographic features of these bluff-forming landslides, such as headscarps, slumped blocks, and hummocky topography, are visible both in the field and in the LiDAR-derived topographic data (Figs. 2 and 3) throughout much of the coastal Puget Sound lowlands.

High-resolution DEMs with 6-ft (1.8-m) point spacing for the Puget Sound lowlands are available from the Puget Sound LiDAR Consortium (http://pugetsoundlidar.ess.washington.edu/). As part of an ongoing landslide hazard project by the Geology and Earth Resources division of the Washington State Department of Natural Resources (WA DNR), M. Polenz (WA DNR, personal communication, 2008) recently compiled a landslide inventory for the marine shores of Thurston County using LiDAR-derived DEMs coupled with aerial photographs and field reconnaissance. The inventory includes both deep-seated and surficial landslides with brief descriptions of more than 800 landslide polygons. In our analysis of the MTC and CBP study areas (Fig. 2), we use only the large, deep-seated landslides, which cover 4% of MTC and 26% of CBP. Schulz (2004, 2005, 2007) created a detailed deep-seated landslide map for the city of Seattle by using LiDAR-derived DEMs and field observations to map headscarps, landslide bodies, and denuded slopes associated with ancient deep-seated landslides. In our analysis of the SEA study area (Fig. 3), we use all three of these features, which cover 15% of SEA.

3. Methods

We utilize two common signal processing techniques — the two-dimensional discrete Fourier transform (2D DFT) and the two-dimensional continuous wavelet transform (2D CWT) — to quantify the topographic expressions of deep-seated landslides and to objectively map their locations in our study areas. Fourier analysis has a rich history in the earth sciences and has been used to quantify

various topographic patterns and landscape-scaling properties (Rayner, 1972; Hanley, 1977; Harrison and Lo, 1996; Perron et al., 2008). Wavelet analysis has recently gained popularity among those studying earth and planetary surface morphology and has successfully been implemented in studies that, for example, analyze polar topography (Malamud and Turcotte, 2001), quantify salmon nesting patterns (McKean et al., 2008), extract channel networks (Lashermes et al., 2007), and analyze morphotectonic lineaments (Jordan and Schott, 2005). The 2D DFT transforms discretely sampled data from the spatial domain to the frequency domain, providing information about

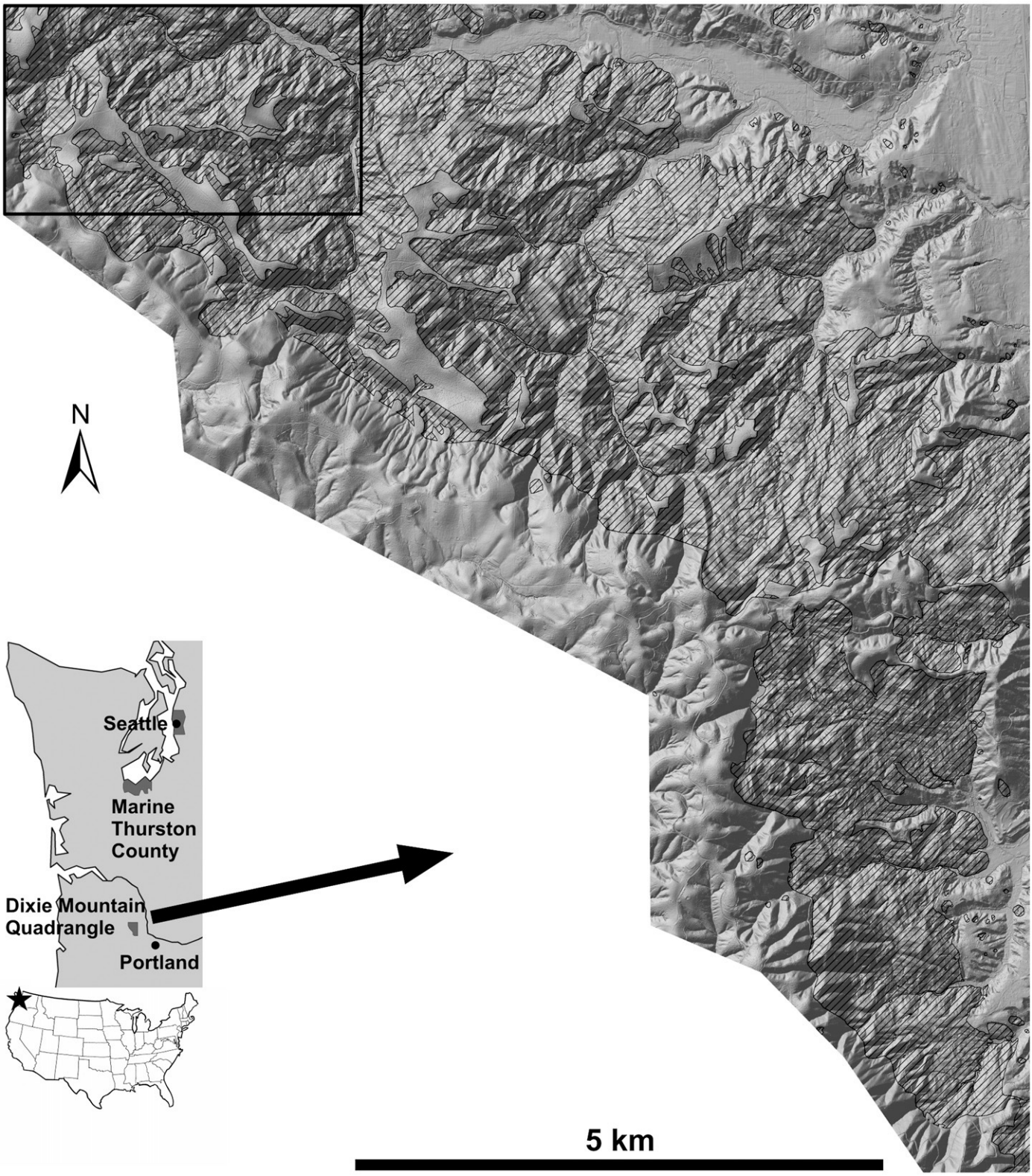

Fig. 1. LiDAR-derived hillshade map of the Dixie Mountain quadrangle, Oregon (DMQ) study area with deep-seated landslides independently mapped by Madin and Niewendorp (2008) shown in black, hatched pattern. The black rectangle in the NW corner outlines the Northwest Dixie Mountain quadrangle (NWD) study area, which we show in detail to illustrate our methods and results in Figs. 5 and 8.

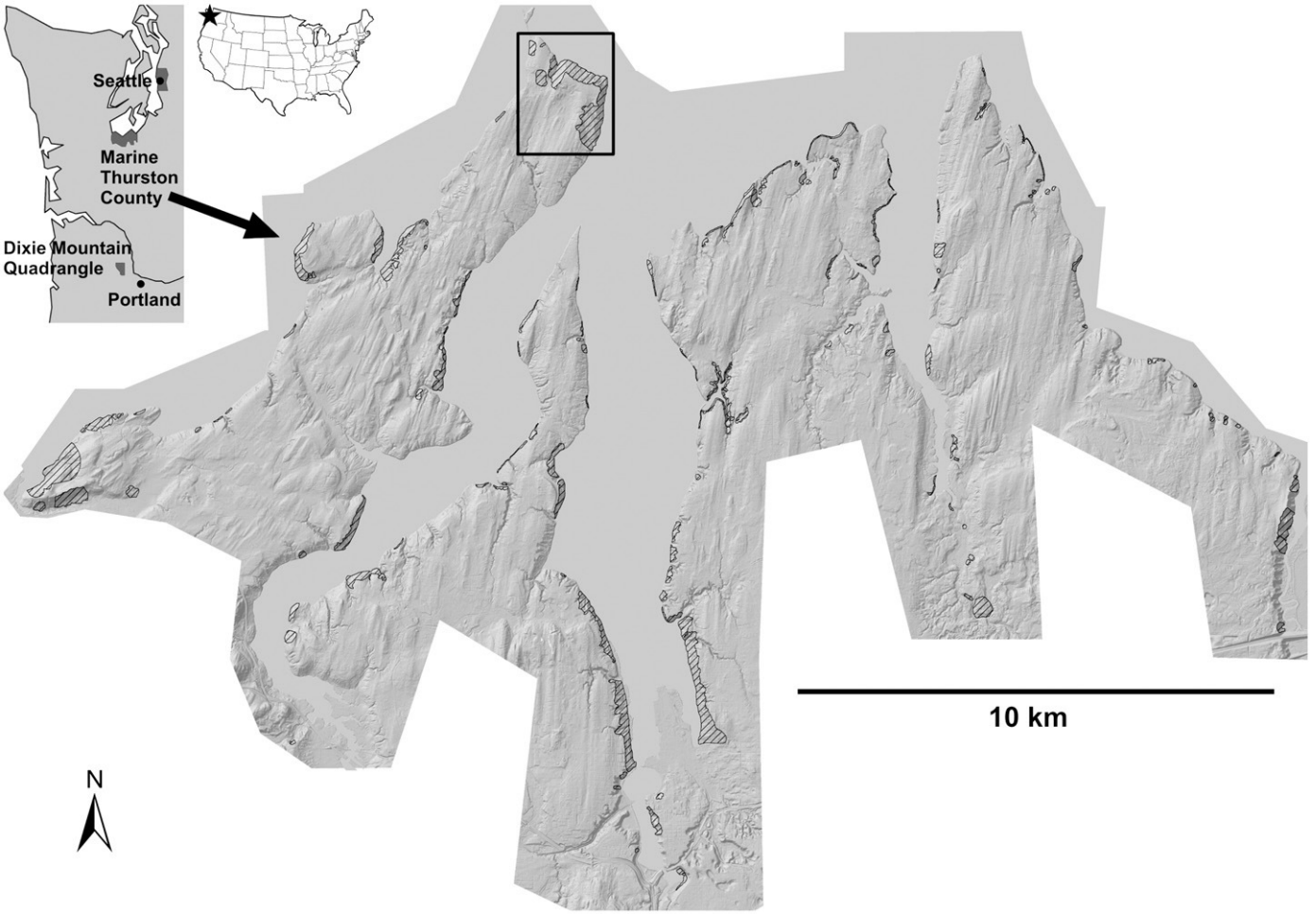

Fig. 2. LiDAR-derived hillshade map of the marine Thurston County, Washington (MTC) study area with deep-seated landslides independently mapped by M. Polenz (WA DNR, personal communication, 2008) shown in black, hatched pattern. The black rectangle in the north-central part of the figure outlines the Carlyon Beach Peninsula (CBP) study area, which we show in detail to illustrate our methods and results in Figs. 6, 9, and 12.

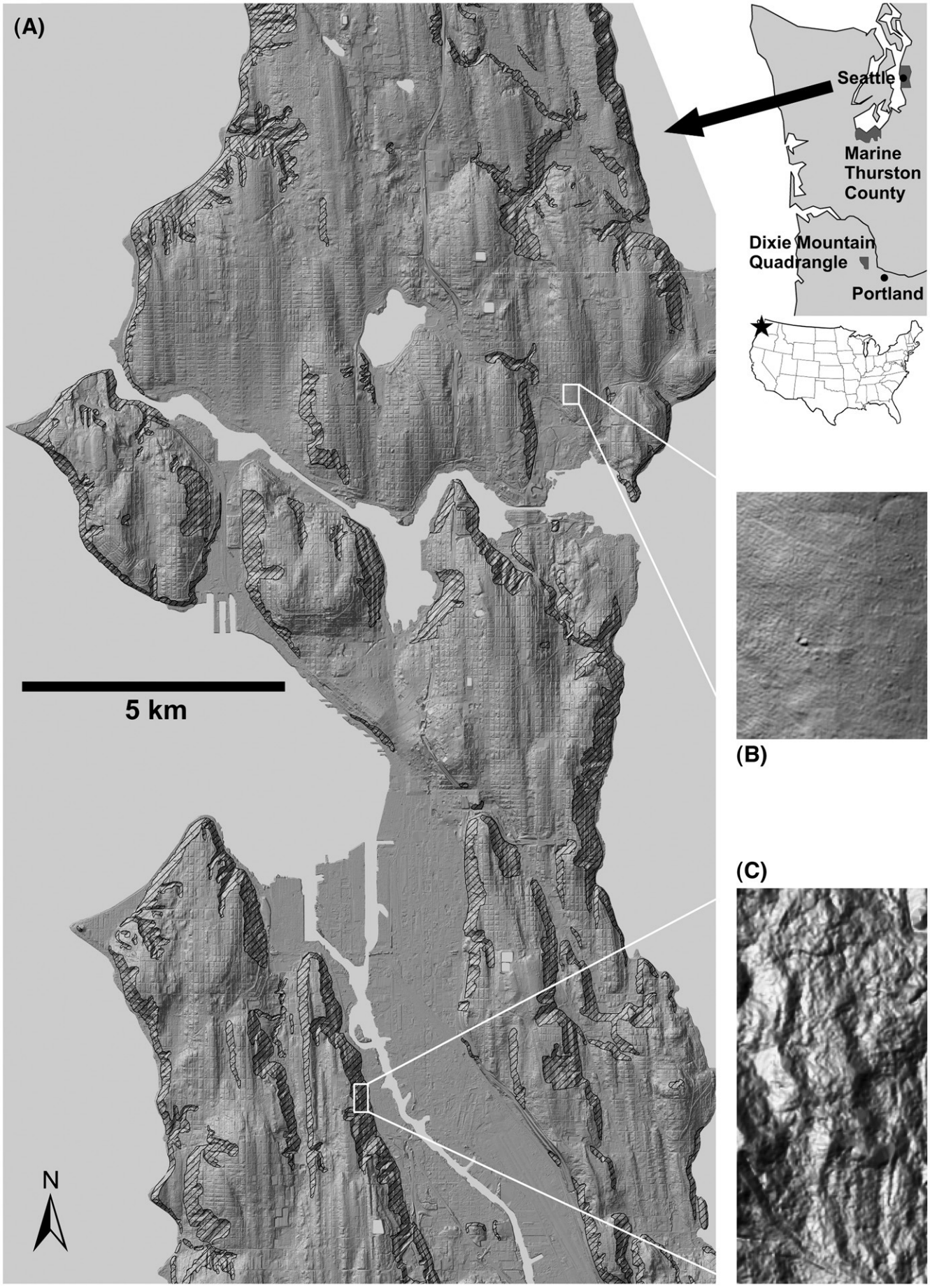
(A)
Seattle
Marine
Thurston
County
Dixie Mountain
Quadrangle
Portland
5 km
N
(B)
(C)

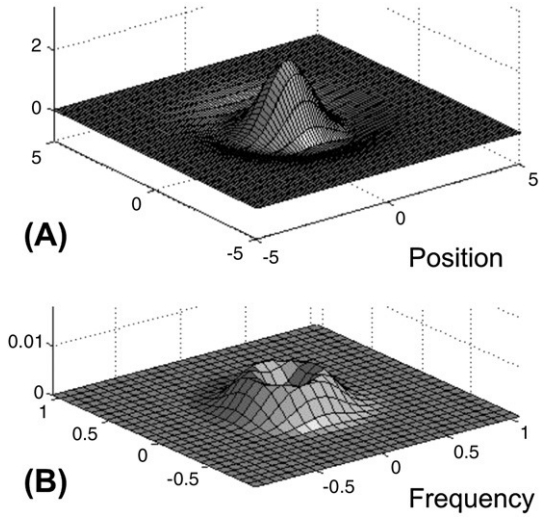

Fig. 4. (A) Two-dimensional Mexican hat wavelet ($s=1$), and (B) its Fourier transform. In (B), radial frequency increases, and wavelength decreases, with distance from the center of the square array. The ring-shaped peak in (B) indicates the dominant frequency of the Mexican hat wavelet, which is the inverse of its wavelength or equivalent spatial scale. Note that in (B) the Mexican hat is spread out and contains additional frequencies on either side of its main frequency.

how the amplitude of topographic features is distributed over a range of spatial frequencies. The 2D CWT transforms spatial data into position-frequency space, providing information about how amplitude is distributed over spatial frequency at each position in the data. We use both these transforms to determine characteristic wavelengths of landslide features and then to map where the signatures of these features are strongest. Throughout this paper we use spatial scale and wavelength interchangeably, and we refer to the inverse of a feature's wavelength as its spatial frequency. To assess the accuracy of our landslide mapping algorithms, we evaluate how well the algorithm outputs match the independently mapped deep-seated landslides in each study area. These independently compiled maps are somewhat subjective as are all landslide inventory maps. However, they were created using previously unavailable high-resolution DEMs in addition to traditional methods and therefore are the most accurate deep-seated landslide maps available for our study areas.

We coded and executed all computations on a desktop computer using Matlab Version 7.4.0 (The MathWorks, Inc.), so the methods should be accessible to all interested parties. Copies of our algorithms are available at http://www.uoregon.edu/~jroering/specmaptools.html.

3.1. 2D DFT

Two-dimensional Fourier analysis of topography provides quantitative information about the amplitude, orientation, and shape of periodic and quasiperiodic features over a range of spatial frequencies (Rayner, 1972; Hanley, 1977; Harrison and Lo, 1996; Perron et al., 2008). The 2D DFT of a data set $z(x,y)$ with $N_x \times N_y$ evenly spaced nodes is (Priestley, 1981; Perron et al., 2008)

$$Z\left(k_x, k_y\right) = \sum_{m=0}^{N_x-1}\sum_{n=0}^{N_y-1} z(m\Delta x, n\Delta y) e^{-2\pi i\left(\frac{k_x m}{N_x}+\frac{k_y n}{N_y}\right)} \quad (1)$$

where k_x and k_y are wavenumbers in the x- and y-directions, Δx and Δy are grid spacings in the x- and y-directions, and m and n are indices in z.

A common way of estimating the power spectrum of Z is the DFT periodogram,

$$V_{\mathrm{DFT}} = \frac{1}{N_x^2 N_y^2}\left|Z(k_x, k_y)\right|^2 \quad (2)$$

which has units of amplitude squared, and when summed over all wavenumbers is equal to the variance of z by Parseval's theorem. The DFT periodogram produces a 2D array of values that describes the amplitudes of the frequency components of z. For the purposes of automated landslide mapping, Eq. (2) therefore provides a measure of the amplitude of the topographic features in a DEM, such as hummocks and slumped blocks, at particular wavelengths and orientations.

3.2. 2D CWT

The generalized 2D CWT of $z(x,y)$ at wavelet scale parameter s and location (a,b) is (Kumar and Foufoula-Georgiou, 1994, 1997; Addison, 2002)

$$C(s,a,b) = \frac{1}{s}\int_{-\infty}^{\infty}\int_{-\infty}^{\infty} z(x,y)\psi\left(\frac{x-a}{s}, \frac{y-b}{s}\right)\mathrm{d}x\mathrm{d}y \quad (3)$$

where ψ represents a wavelet family. The 2D CWT is a convolution of z and ψ, and thus the wavelet coefficient $C(s,a,b)$ provides a measure of how well the wavelet ψ matches the data z at each node. When s is large, ψ is spread out and takes into account long wavelength features of z; when s is small, ψ is more localized in space and sensitive to fine-scale features of z. We follow the convention of defining the wavelength or equivalent spatial scale of ψ as the inverse of its band-pass frequency (Kumar and Foufoula-Georgiou, 1997; Torrence and Compo, 1998), as illustrated in Fig. 4.

Because its shape resembles that of a landslide hummock, we use the 2D Mexican hat wavelet, described by the following equation and illustrated in Fig. 4, for our analyses:

$$\psi(x,y) = \left(2 - x^2 - y^2\right)e^{-\frac{1}{2}\left(x^2+y^2\right)} \quad (4)$$

The Mexican hat is proportional to the second derivative of a Gaussian envelope and has a wavelength of $2\pi s/(5/2)^{1/2}$ times the grid spacing (Torrence and Compo, 1998). Convolving the 2D Mexican hat wavelet with a topographic data set therefore precisely maps features of specific wavelengths and amplitudes, including characteristic landslide features.

The 2D CWT can also be condensed into a power spectrum by computing its variance over $N_a \times N_b$ nodes at each wavelet scale (Percival, 1995):

$$V_{\mathrm{CWT}}(s) = \frac{1}{2N_a N_b}\sum_a\sum_b \left|C(s,a,b)\right|^2 \quad (5)$$

Similar to a Fourier power spectrum, Eq. (5) provides a general measure of how the amplitude of features changes with frequency over an entire data set. However, as shown for the 2D Mexican hat wavelet in Fig. 4, a wavelet of a given scale typically contains a range of frequencies on either side of its main band-pass frequency. Analyzing a single wavelet scale with the continuous wavelet transform is therefore sensitive to a range of frequencies, while the discrete Fourier transform analyzes individual frequencies separately. This has the effect of smoothing the peaks in a wavelet power spectrum compared to its Fourier counterpart (Torrence and Compo, 1998).

3.3. Fourier and wavelet spectra

To determine the characteristic wavelengths of deep-seated landslide features in each study area, we first select representative

Fig. 3. (A) LiDAR-derived hillshade map of the Seattle, Washington (SEA) study area, with deep-seated landslides independently mapped by Schulz (2004, 2005, 2007) shown in black, hatched pattern. Boxes (B) and (C) indicate the patches of unfailed and failed terrain, respectively, used to compute the power spectra described in Section 3.3 and shown in Fig. 7 for the SEA study area.

patches of mapped deep-seated landslides and unfailed terrain. In Seattle, we use a portion of the Riverview landslide and the glacially sculpted upland surface of Calvary Cemetery as representative patches (Fig. 3B and C). For the Dixie Mountain quadrangle, we use a section of the Dutch Canyon landslide complex and a nearby smooth, loess-mantled surface (Fig. 5). For marine Thurston county, we use the historically active Carlyon Beach landslide and the neighboring glacially sculpted upland surface (Fig. 6).

Next, we normalize each patch of terrain to have unit variance and generate Fourier and wavelet power spectra using Eqs. (2) and (5), respectively (Fig. 7A–C, G–I). For easier visualization, we condense the 2D array produced by Eq. (2) to a 1D power spectrum by plotting V_{DFT} against radial frequency $(f_x^2+f_y^2)^{1/2}$. The spectra all show spectral power decreasing with spatial frequency, but the spectra tend to diverge over specific ranges of frequencies. In the DFT-generated spectra, unfailed terrain tends to have higher spectral power at high frequencies, and deep-seated landslides tend to have higher spectral power at intermediate frequencies. In the CWT-generated spectra, both types of terrain have similar spectral power at low and high frequencies, but deep-seated landslides tend to have higher spectral power at intermediate frequencies. These patterns indicate that deep-seated landsliding in our study areas tends to transfer spectral power from low and high frequencies to intermediate frequencies. Mechanisms that concentrate spectral power include failure of coherent blocks of material separated by scarps in the upper portion of the landslides and folding from compressive stress in the lower portions.

To more clearly highlight the frequency bands over which deep-seated landslides tend to concentrate spectral power, we normalize the landslide-generated spectra by their corresponding unfailed surface-generated spectra (Fig. 7D–F, J–L). All six normalized spectra produce well-defined peaks that indicate the characteristic wavelengths of deep-seated landslide features in similar substrates in each study area. The peaks of the spectra indicate a characteristic wavelength of ~22 m for the Dixie Mountain quadrangle and Seattle, and ~32 m for marine Thurston County, with negligible differences in peak location between the Fourier and wavelet spectra.

Because landslide features occur over a range of wavelengths in both study areas, as indicated by both observation and Fig. 7, we take the full width at half maximum (FWHM) of each peak as a straightforward measure of the spectrum's spread and use this characteristic band of spatial frequencies in our mapping algorithms. For the Dixie Mountain quadrangle, the Fourier and wavelet spectra indicate characteristic frequency bands of ~0.029 to 0.055 m^{-1} (wavelengths of ~18 to 34 m) and of ~0.022 to 0.09 m^{-1} (wavelengths of ~11 to 45 m), respectively. For marine Thurston County, the normalized Fourier spectrum indicates a characteristic frequency

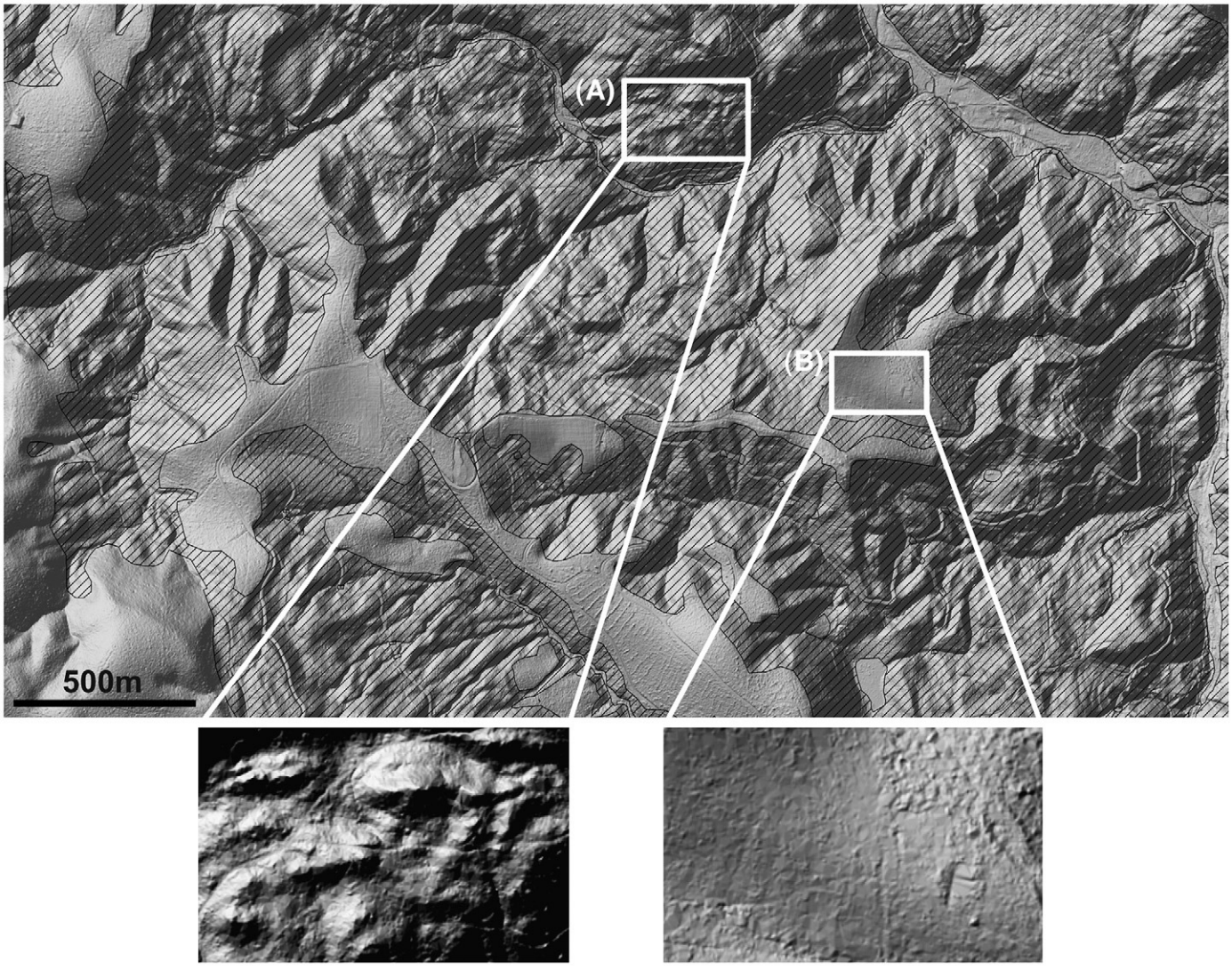

Fig. 5. LiDAR-derived hillshade map of the NWD study area with independently mapped, deep-seated landslides (Madin and Niewendorp, 2008) shown in black, hatched pattern. White boxes (A) and (B) indicate the patches of landslide and unfailed terrain, respectively, used to compute the normalized power spectra described in Section 3.3 and shown in Fig. 7 for the NWD and DMQ study areas.

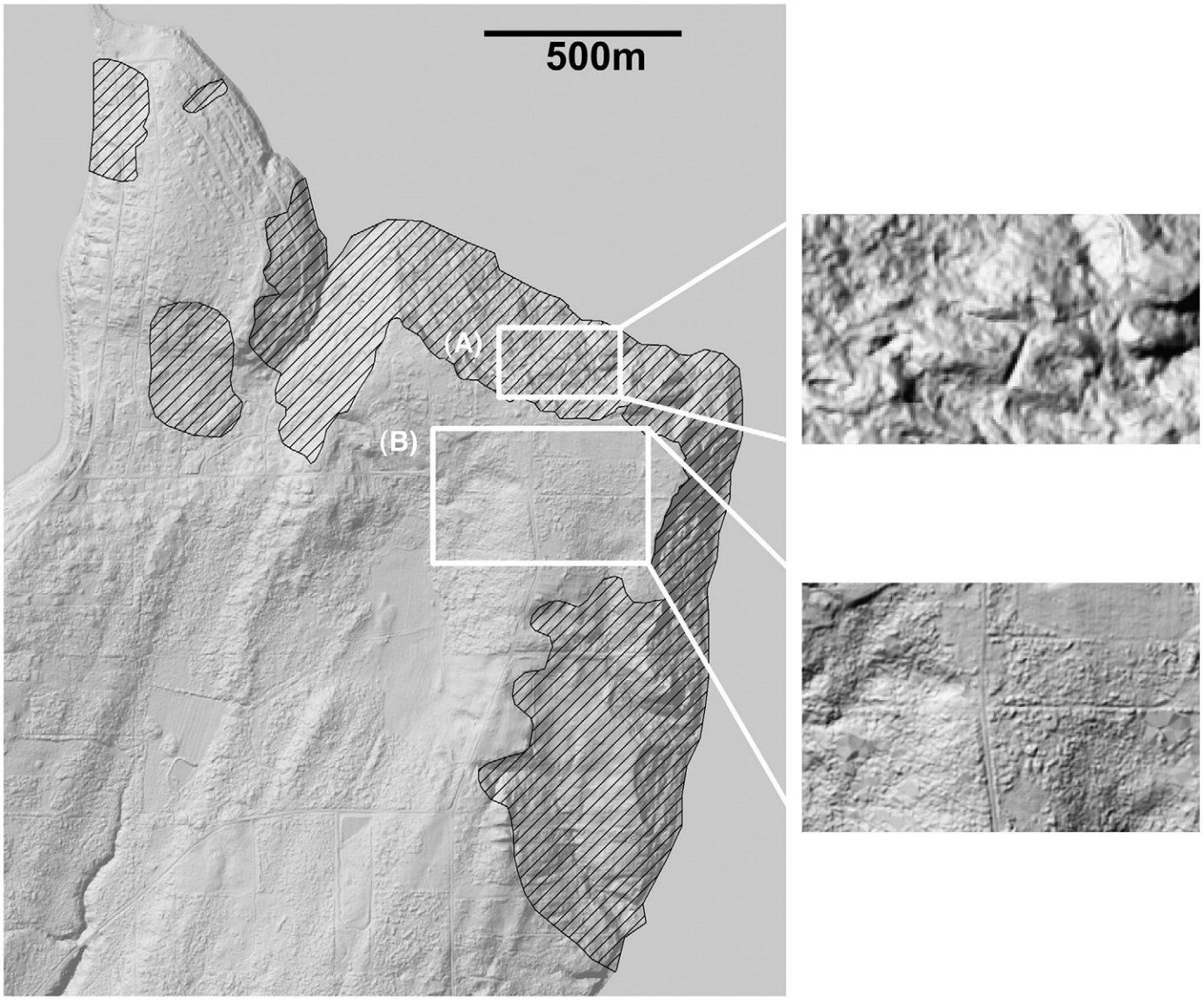

Fig. 6. LiDAR-derived hillshade map of the CBP study area with independently mapped, deep-seated landslides (M. Polenz, WA DNR, personal communication, 2008) shown in black, hatched pattern. White boxes (A) and (B) indicate the patches of landslide and unfailed terrain, respectively, used to compute the power spectra described in Section 3.3 and shown in Fig. 7 for the CBP and MTC study areas.

band of ~0.020 to 0.048 m^{-1} (wavelengths of ~21 to 50 m), while the normalized wavelet spectrum indicates a band of frequencies from ~0.020 to 0.09 m^{-1} (wavelengths of ~11 to 50 m). In Seattle, the normalized Fourier spectrum defines a characteristic frequency band of ~0.030 to 0.053 m^{-1} (wavelengths of ~19 to 33 m), and the normalized wavelet spectrum defines a band of frequencies from ~0.020 to 0.090 m^{-1} (wavelengths of ~11 to 50 m). At all three sites, the FWHM is broader in the wavelet spectrum because each wavelet scale consists of a range of frequencies. At small wavelet scales in particular, the Mexican hat wavelet becomes more spread out in the frequency domain, causing the right-hand sides of the wavelet spectra in Fig. 7 to differ considerably from their analogous Fourier spectra.

3.4. Mapping spectral power

In order to automatically map terrain with features indicative of past deep-seated landslides, we map spatial patterns of spectral power contained within the frequency bands determined from Fig. 7 using the transforms described in Sections 3.1 and 3.2.

3.4.1. Windowed 2D DFT

To map spatial patterns of spectral power with Fourier analysis, we implement the 2D DFT in a windowed mode. The algorithm systematically works its way through the DEM computing the DFT periodogram using Eq. (2) within a square window centered on each node. The values of the periodogram calculated at each node are then summed over the characteristic frequency band, and this spectral power sum is displayed in mapview for analysis. A node with a high spectral power sum indicates a strong topographic signature of deep-seated landsliding within the window surrounding that node.

For both study areas we use a 63-by-63 node window, corresponding to a 115-by-115 m square of terrain in the Puget Sound lowlands (study areas MTC, CBP, and SEA) and a 58-by-58 m square of terrain in the Dixie Mountain quadrangle (study areas DMQ and NWD). In a window this size, the 2D DFT samples 64 evenly spaced frequencies ranging from zero to $(2\Delta)^{-1}$, the Nyquist frequency, in both the *x*- and *y*-directions, placing the frequencies of interest near the middle of the spectrum. This choice of window size also represents a balance between sampling enough frequencies to sufficiently describe the terrain and keeping computation times reasonable.

3.4.2. 2D CWT

Because wavelet analysis preserves information about both scale and position, we implement Eq. (3) directly to map spatial patterns of spectral power with the 2D CWT. We identify wavelet scales corresponding to the minimum and maximum frequencies in each study area's characteristic frequency band (Fig. 7J–L) and analyze only integer wavelet scales between and including these bounds. This choice of scales adequately encompasses the frequencies of interest in each landscape while keeping computation times short. The algorithm first computes a wavelet coefficient at each node in the DEM at each wavelet scale. It then squares and sums the computed wavelet coefficients at each node and displays the outcome in mapview. A node with a high value indicates topography characteristic of a deep-seated landslide at that node. Because the 2D CWT is not windowed as is our 2D DFT algorithm, we smooth the output of our 2D CWT algorithm by averaging within a 63-node diameter window in order to produce comparable maps that illustrate broad patterns of past deep-seated slope instability.

3.5. Optimizing algorithm outputs

The most straightforward way to translate an array produced by the algorithms described in Sections 3.4.1 and 3.4.2 into a deep-seated landslide map is to classify each node in the array as a landslide if its spectral power sum is above a cutoff value or as an unfailed surface if its value is below the cutoff. This approach does not delineate boundaries of individual landslides that border or overlap each other, but instead

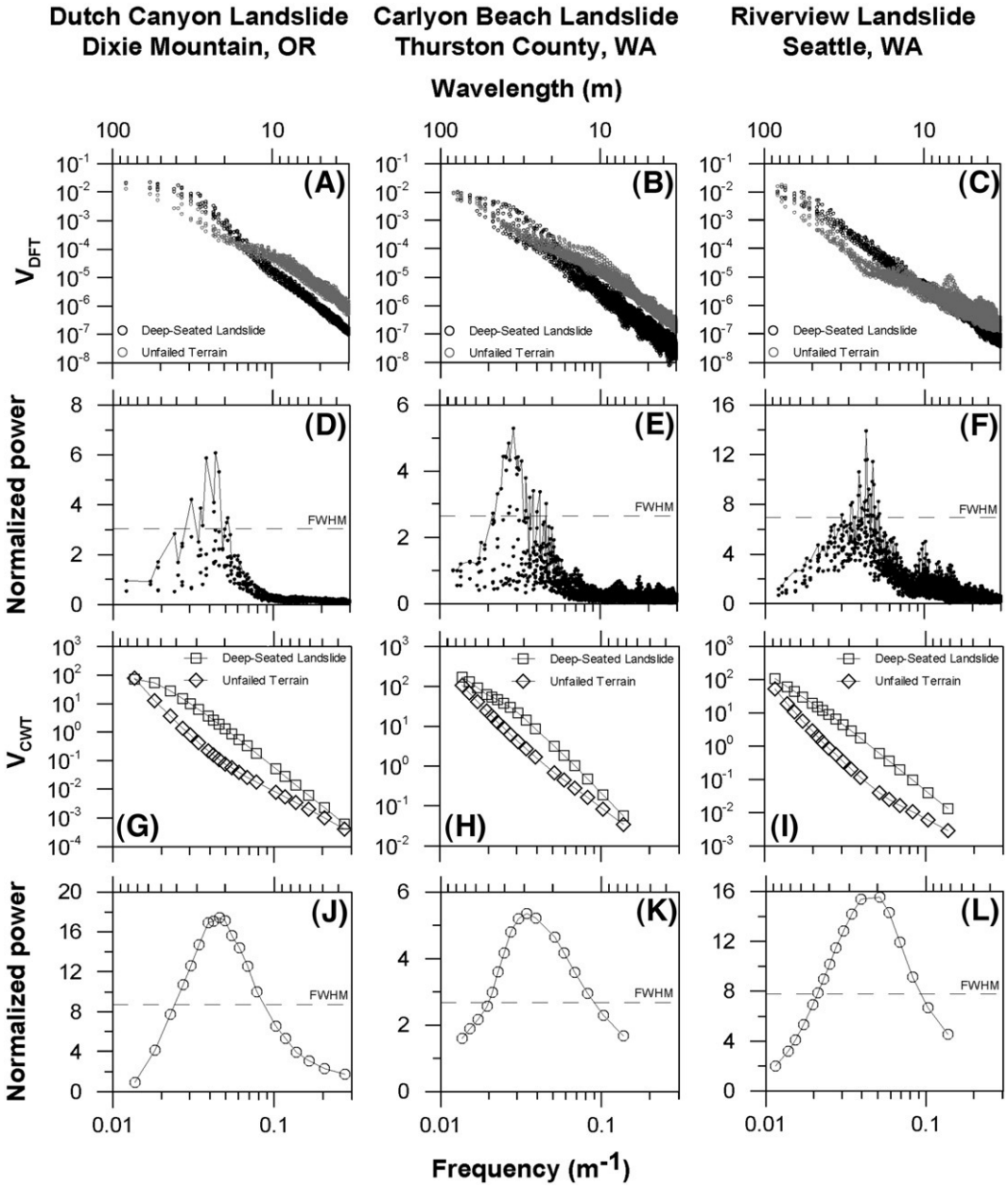

Fig. 7. Power spectra indicating the frequency bands characteristic of deep-seated landslides in the DMQ and NWD study areas (left-hand column), the MTC and CBP study areas (center column), and the SEA study area (right-hand column). Fourier power spectra (A–C) show that spectral power tends to decrease with increasing frequency in both unfailed and deep-seated landslide terrain. The peaks of the normalized Fourier spectra (D–F) highlight discrepancies in spectral power between deep-seated landslides and unfailed terrain, indicating the range of frequencies over which deep-seated landslides tend to concentrate spectral power. Solid lines highlight the upper envelopes of the normalized spectra, and dashed lines indicate the full width at half maximum (FWHM) for each spectrum. The wavelet power spectra (G–I) confirm that spectral power decreases with frequency, and the peaks of the normalized wavelet spectra (J–L) also highlight the bands of frequencies over which deep-seated landslides concentrate spectral power. All patches of terrain were normalized to have unit variance before computing spectral power.

indicates all nodes in the study area that have the topographic signature of deep-seated landsliding. The map resulting from a given cutoff value can then be compared to the independently mapped deep-seated landslides. Following Carrara et al. (1992), we select optimal cutoff values for each study area based on the overall error index

$$E = \frac{(A_1 \cup A_2) - (A_1 \cap A_2)}{(A_1 \cup A_2)}, \quad 0 \le E \le 1 \tag{6}$$

where A_1 and A_2 are the areas of landslides in the two maps being compared, and $\cup$ and $\cap$ represent the geometric union and intersection, respectively. The geometric union counts the total area of deep-seated landslides identified by the landslide inventory or by our algorithms, while the geometric intersection counts the total area identified as a deep-seated landslide by both the inventory and our algorithms. We compute E for each output array in each study area over a range of cutoff values, and select the best algorithm-produced landslide inventory map using the cutoff value that minimizes E. Nodes that contain no data or are located within a body of water are not included in our optimization routines.

4. Results

4.1. Landslide maps

Arrays produced by applying our 2D DFT and 2D CWT algorithms to the study areas clearly highlight variations in spectral power contained in wavelengths characteristic of deep-seated landslides across broad areas of terrain (Figs. 8A and B, 9A and B, and 10A and C). Spectral power sums vary by orders of magnitude over each study area, reflecting considerable variation in the topography. Areas that are smooth over the range of spatial frequencies being analyzed (Fig. 7) have low spectral power, while areas that are rough over this frequency band have high spectral power. These areas of high spectral power tend to coincide with mapped deep-seated landslides, verifying that a cutoff spectral power sum can delineate landslide terrain.

In our five study areas, selecting an optimal cutoff spectral power sum by minimizing the error index correctly classifies an average of 82% of the land area as compared to the independently compiled landslide inventories (Table 1). The minima of the error index curves (Fig. 11) clearly indicate optimal cutoff spectral power sums for each study area. To the left of the minimum in each error index curve, large numbers of unfailed nodes are incorrectly classified as landslide nodes, keeping E high. To the right of the minimum, E is again high, but this time from landslide nodes being misclassified as unfailed nodes. In the vicinity of the optimal cutoff values, the error index curves are markedly lower in the Dixie Mountain quadrangle (DMQ and NWD) than in the Puget Sound lowlands (MTC, CBP, and SEA) because landslides occupy a majority of the area in the Dixie Mountain quadrangle and only a small fraction of the area in the Puget Sound lowland study areas. Defining the best cutoff value as the spectral power sum that minimizes E produces visually appealing landslide maps (Figs. 8C and D, 9C and D, and 10B and D) and correctly classifies a high percentage of the land surface in our study areas (Table 1).

The error index curves shown in Fig. 11 and optimal cutoff values shown in Table 1 also highlight how the sizes of our data sets affect the optimal cutoff spectral power sums. Optimal cutoff values are similar for MTC, SEA, and CBP and for DMQ and NWD, but tend to be higher in the larger study areas. Our larger study areas tend to have higher percentages of terrain mapped as unfailed, and this unfailed terrain

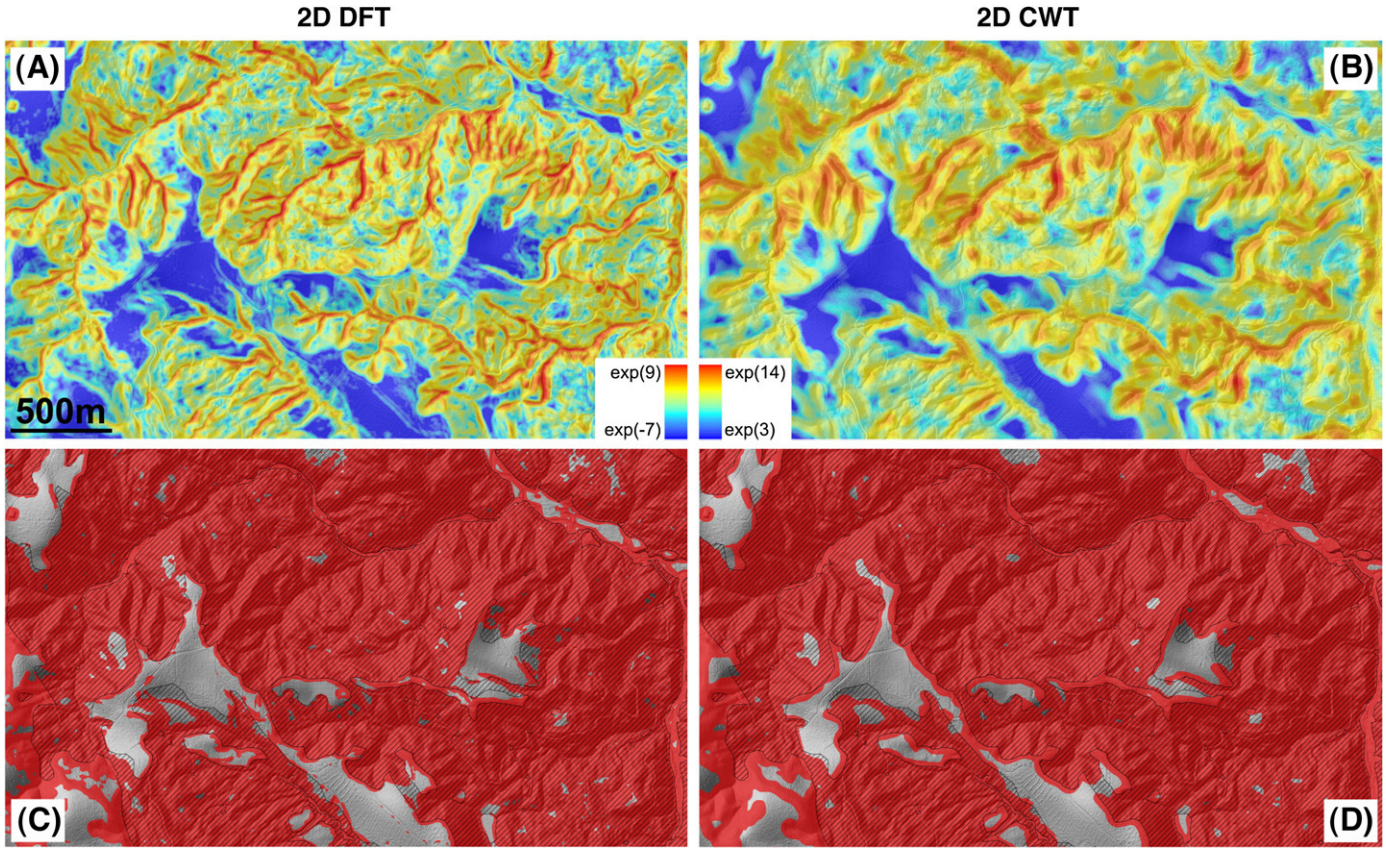

Fig. 8. Spectral power sums from the (A) 2D DFT and (B) 2D CWT and their corresponding optimally classified landslide maps (C and D) for the NWD study area. Warm colors (A and B) indicate strong topographic signals of deep-seated landslide terrain, while shaded red areas (C and D) delineate landslide terrain based on the optimal cutoff values (Table 1). Independently mapped deep-seated landslides (Madin and Niewendorp, 2008) are overlain in the black, hatched pattern. (For interpretation of the references to color in this figure legend, the reader is referred to the web version of this article.)

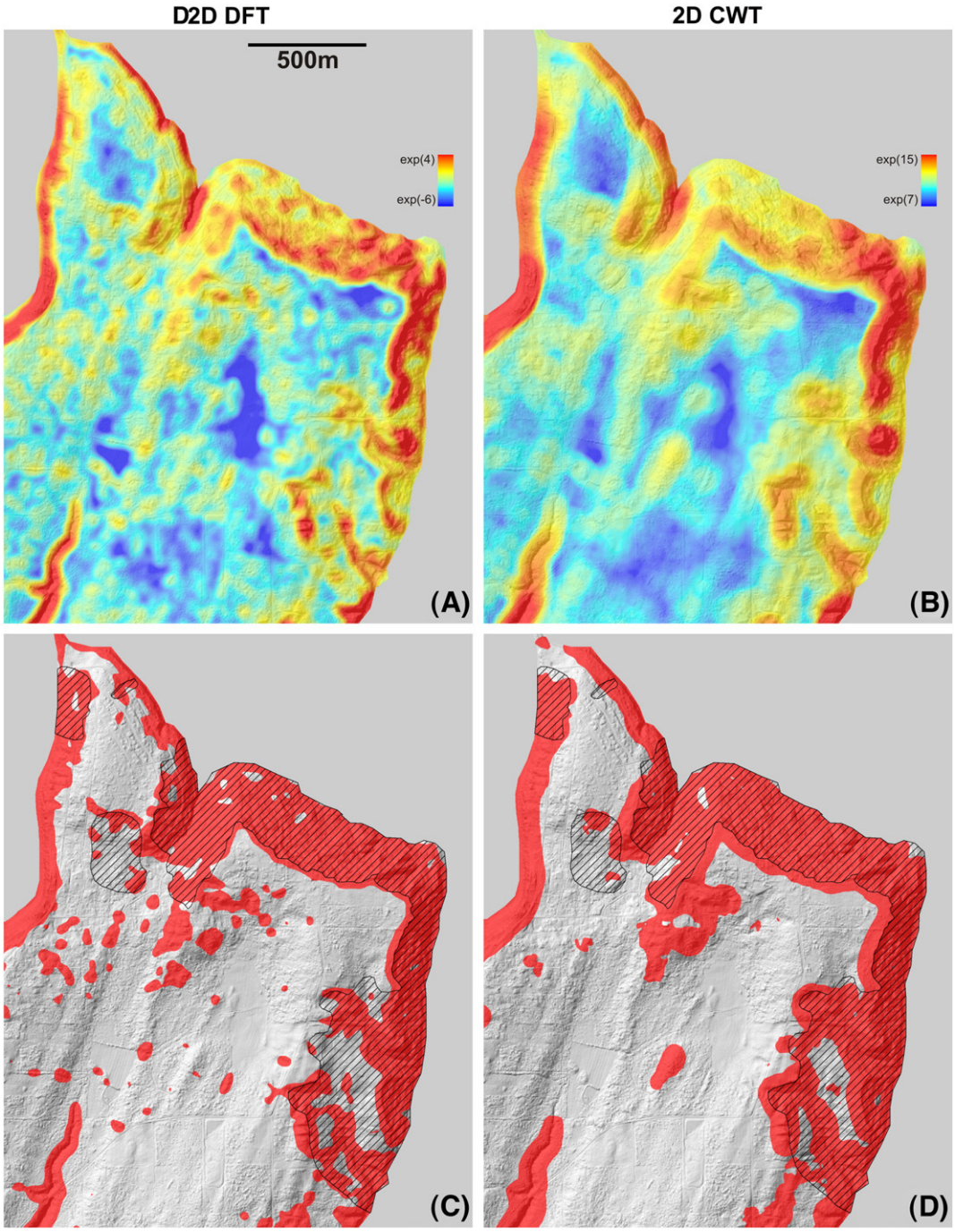

Fig. 9. Spectral power sums from the (A) 2D DFT and (B) 2D CWT and their corresponding optimally classified landslide maps (C and D) for the CBP study area. Warm colors (A and B) indicate strong topographic signals of deep-seated landslide terrain, while shaded red areas (C and D) delineate landslide terrain based on the optimal cutoff values (Table 1). Independently mapped deep-seated landslides (M. Polenz, WA DNR, personal communication, 2008) are overlain in the black, hatched pattern. (For interpretation of the references to color in this figure legend, the reader is referred to the web version of this article.)

inevitably has some topographic features that our algorithms interpret as deep-seated landslides, as discussed in the following paragraphs. Higher cutoff spectral power sums reduce the number of nodes in these large areas of unfailed terrain that are incorrectly classified as landslide nodes.

Although the optimized landslide maps produced by our algorithms succeed in mapping a large majority of the terrain in each study area correctly, some systematic misclassifications occur. The algorithms tend to falsely classify topographic features with sharp edges or spatial frequencies in the characteristic landslide band as landslide nodes. Conversely, the algorithms tend to overlook topographic features within the boundaries of known landslides that have subdued amplitudes due to non-landslide erosive processes or human modification of the landscape.

In our study areas, sharp-edged topographic features that tend to be misclassified as deep-seated landslides include narrow valley bottoms between landslide masses (north-central Fig. 8C and D), ravines (SW corner of Fig. 9C and D), edges of steep bluffs lacking deep-seated landslides (western Fig. 9C and D), and some roads (small arrow, Fig. 10B and D). These sharp edges produce high spectral power in Fourier analysis because large amplitude sine and cosine waves over a range of frequencies are required to capture abrupt

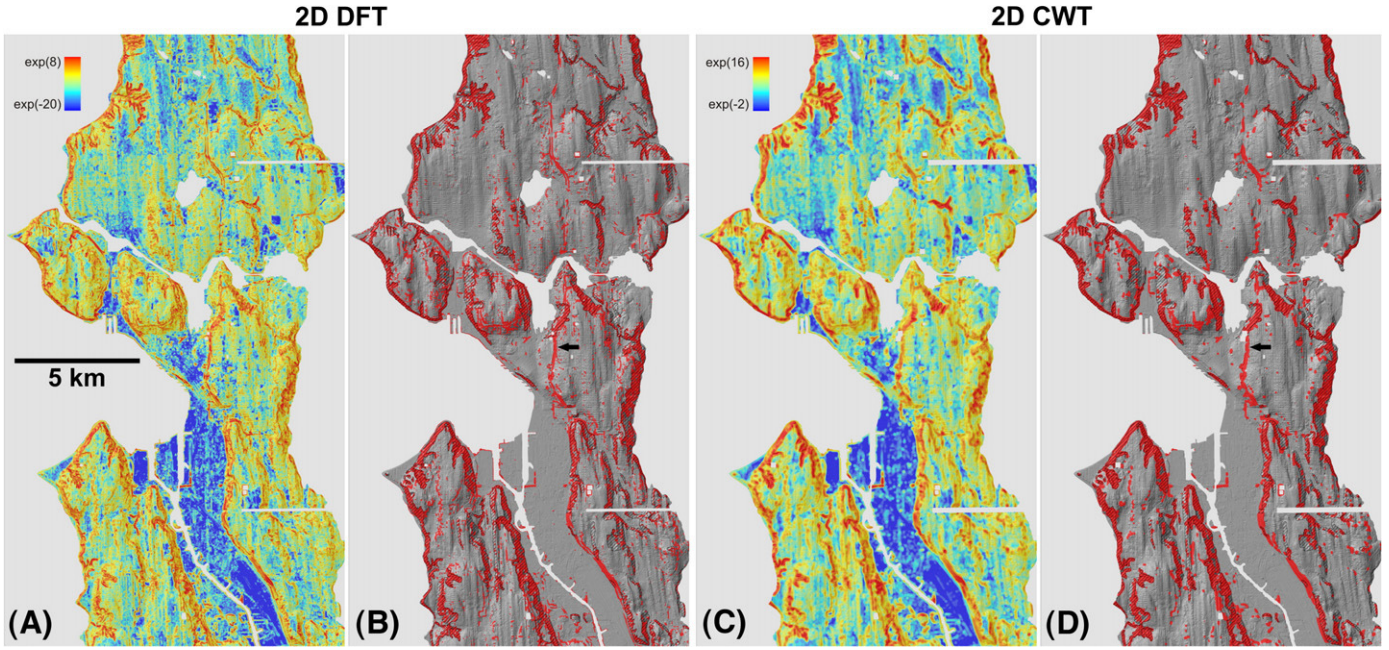

Fig. 10. Spectral power sums from the (A) 2D DFT and (C) 2D CWT and their corresponding optimally classified landslide maps (B and D) for the SEA study area. Warm colors (A and C) indicate strong topographic signals of deep-seated landslide terrain, while shaded red areas (B and D) delineate landslide terrain based on the optimal cutoff values (Table 1). Independently mapped deep-seated landslides (Schulz, 2004, 2005, 2007) are overlain in the black, hatched pattern. Small, black arrows (B and D) indicate the location of Interstate 5, which runs N–S through the study area and produces high spectral power sums because of its sharp edges. Grey, horizontal bars on the right-hand side of each image are areas of no data because of gaps in the LiDAR coverage. (For interpretation of the references to color in this figure legend, the reader is referred to the web version of this article.)

Table 1
Comparing algorithm-generated and independently compiled deep-seated landslide maps in each study area.

	Method	Study area				
		MTC	SEA	CBP	DMQ	NWD
Cutoff value (m^2)	2D DFT	2.86	1.88	0.65	0.33	0.22
	2D CWT	2.6e+5	1.7e+5	5.9e+4	8.7e+3	5.3e+3
Error index	2D DFT	0.84	0.57	0.48	0.39	0.14
	2D CWT	0.86	0.55	0.47	0.39	0.15
Percent correct (%)	2D DFT	88.8	87.1	81.3	68.3	87.0
	2D CWT	86.1	87.8	80.5	67.8	86.0
Correctly classified						
Landslide area (km^2)	2D DFT	3.9	21.8	0.7	32.2	5.2
	2D CWT	4.2	22.6	0.8	32.3	5.3
Unfailed area (km^2)	2D DFT	152.8	163.2	2.1	11.9	0.7
	2D CWT	147.7	163.2	2.0	11.4	0.6
Incorrectly classified						
Landslide area (km^2)	2D DFT	2.9	9.9	0.2	1.9	0.2
	2D CWT	2.5	8.7	0.1	1.8	0.1
Unfailed area (km^2)	2D DFT	16.9	17.6	0.5	18.5	0.7
	2D CWT	22.0	17.1	0.5	19.0	0.8
Total area analyzed (km^2)	2D DFT	176.4	212.5	3.5	64.5	6.8
	2D CWT	176.4	211.1	3.5	64.5	6.8

changes in the data being analyzed. Any window in our analysis that contains an abrupt change in elevation therefore has an abnormally high spectral power sum. Wavelet analysis with the Mexican hat wavelet also tends to highlight sharp edges because of their high curvature. The Mexican hat wavelet is the second derivative of a Gaussian envelope, so convolving a data set with the Mexican hat is akin to computing the data set's second derivative over a length scale proportional to the wavelet scale (Lashermes et al., 2007).

Topographic features in our study areas with wavelengths in the band characteristic of deep-seated landslides include some glacial features of the Puget Sound lowlands (center of Fig. 9C and D) and some fluvially dissected hillslopes in the Dixie Mountain quadrangle. Because these features have large amplitudes over the same wavelengths as deep-seated landslides, they produce high spectral power sums that lead to misclassification as landslide terrain.

In both study areas, landslides have a range of ages and activity levels, so the surfaces of different landslides have undergone different degrees of post-failure modification. Diffusive soil transport processes have likely subdued the topographic expression of many of the older landslides, shifting spectral power to longer wavelengths and making them difficult for our algorithms to detect. For example, our algorithms fail to capture part of the interior of the landslide mapped in the NE corner of Fig. 8C and D, and incorrectly classify the broad patch of smooth topography mapped as an ancient (M. Polenz, WA DNR, personal communication, 2008) deep-seated landslide in the SE corner of Fig. 9C and D. Anthropogenic modification of the landscape has also subdued many landslide morphologic features in our study areas, especially in the Puget Sound lowlands. Development within the mapped landslides on the slopes adjacent to the inlet on the northern shore of the Carlyon Beach peninsula (Fig. 9), for example, has likely removed many landslide features, preventing our algorithms from matching the mapped landslides in this area.

Despite these effects, our results show that automated landslide mapping methods can produce landslide maps with high degrees of precision in our study areas. The normalized spectra in Fig. 7 faithfully indicate the characteristic wavelengths of landslide morphologic features in similar substrates in each study area. The summed spectral power contained within these wavelengths quantifies the topographic signature of deep-seated landsliding at each node in a data set, allowing past deep-seated slope instability to be mapped.

4.2. Dominant wavelength map

In addition to analysis of broad spatial patterns, our methods allow node-by-node analysis of specific topographic features through the production of a dominant wavelength map. To produce the map, we compute wavelet coefficients using Eq. (3) for each study area over a range of wavelet scales and determine the mean wavelet coefficient over the entire area at each scale. The wavelet coefficients are then normalized by the mean at each scale, and the scale with the highest normalized wavelet coefficient is mapped as the dominant spatial scale at each node.

Fig. 12 shows the spatial distribution of dominant wavelength for mapped landslides in the CBP study area. Variations in dominant wavelength within the boundaries of these deep-seated landslides clearly highlight differences in landslide style and geomorphic processes. Most of the terrain within the historically active Carlyon Beach landslide (Fig. 12A) has dominant wavelengths within the characteristic band of ~11 to ~50 m indicated by our normalized wavelet power spectrum (Fig. 7K). Very few nodes within the landslide are dominated by very short or very long wavelengths, illustrating the tendency of deep-seated landsliding to shift spectral power to intermediate wavelengths. This may suggest that the initial deep-seated movement of the landslide occurred recently enough for its topographic signature to remain intact or that continued activity of the landslide has maintained its characteristic topographic expression. Nodes with similar dominant wavelength values

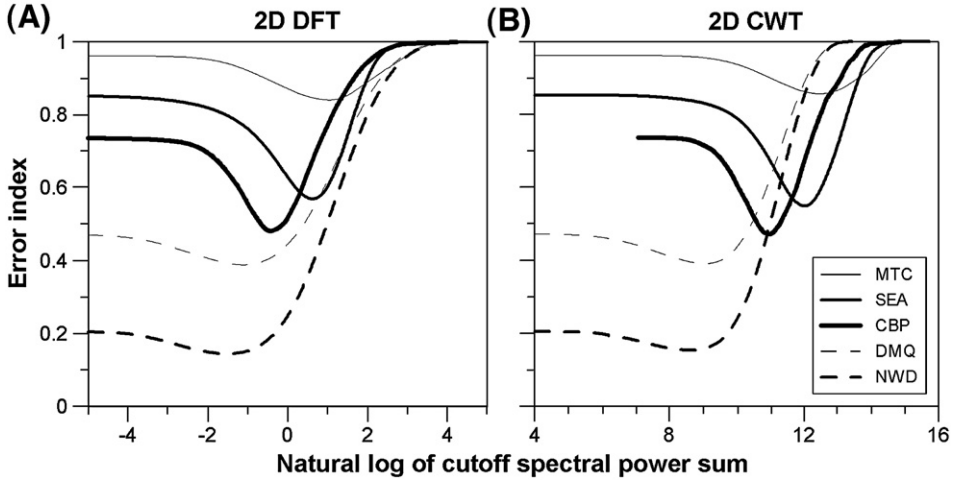

Fig. 11. Error index curves used to select optimal cutoff spectral power sums for classifying each algorithm-generated array with the (A) 2D DFT and the (B) 2D CWT. We computed *E* using 1500 logarithmically spaced cutoff values ranging from the minimum to maximum value in each array.

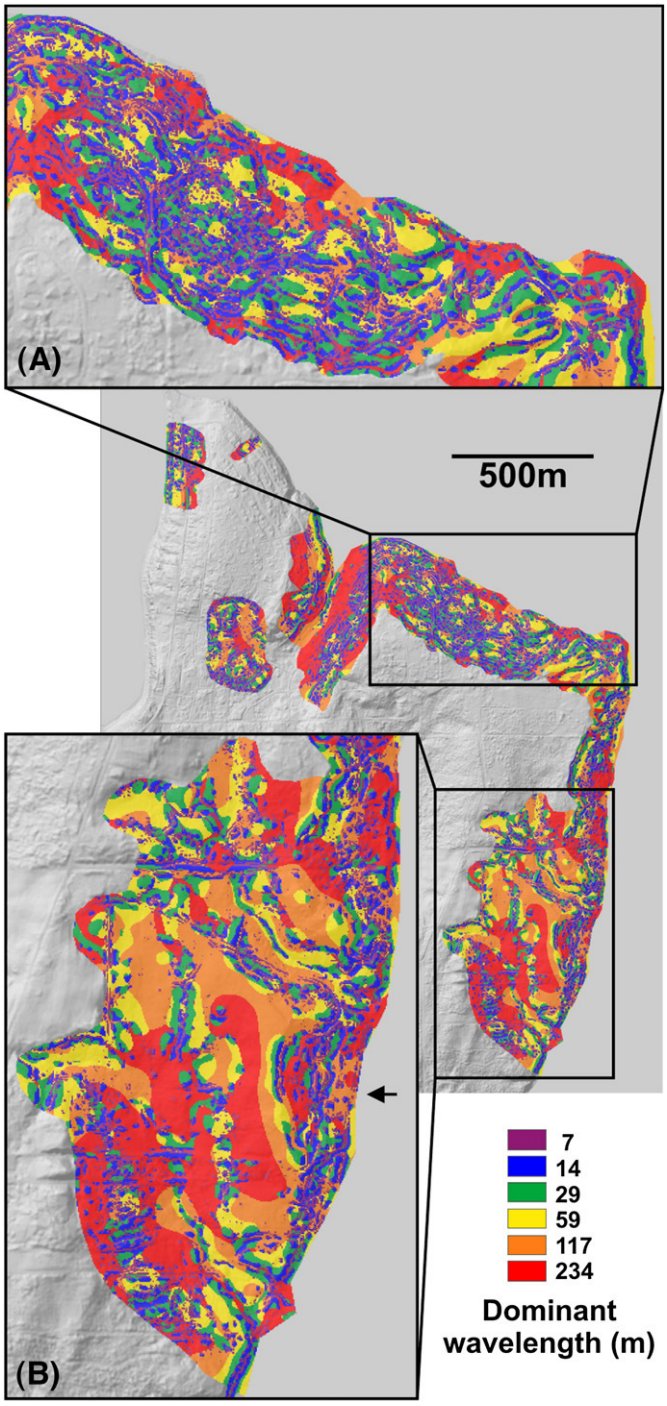

Fig. 12. Dominant wavelength map for deep-seated landslides in study area CBP. Warmer colors indicate longer dominant wavelengths. Recently active landslides (A) tend to have dominant wavelengths in agreement with the FWHM of the power spectra for the CBP study area (Fig. 7K). Ancient (M. Polenz, WA DNR, personal communication, 2008) landslides (B) have longer dominant wavelengths, marking a transition from deep-seated landslide processes to other geomorphic processes. (For interpretation of the references to color in this figure legend, the reader is referred to the web version of this article.)

within the landslide also tend to form continuous bands perpendicular to the local slope. These bands appear to reflect zones of tensile failure and block rotations that result from downslope movement of relatively coherent slide masses. These patterns in dominant wavelength differ from patterns in a nearby ancient (M. Polenz, WA DNR, personal communication, 2008) deep-seated landslide (Fig. 12B). At that site, longer wavelengths tend to dominate most nodes within the ancient landslide, marking a transition from deep-seated landsliding to subsidiary geomorphic processes. Specifically, diffusive soil transport processes appear to have reduced the amplitude of short wavelength features, leaving only longer wavelength expressions of past deep-seated landsliding, except where the landslide has been partly reactivated (small arrow, Fig. 12B). Also, fluvial processes acting in several channels have begun to dissect the ancient landslide mass at a larger spatial scale. Several of the long wavelength bands in the southern half of the ancient landslide trend NNW while the shoreline trends NNE. This likely reflects the dominant direction of fluvial transport and slope modification across the ancient landslide surface or indicates that large-scale blocks in the landslide failed in a direction not perpendicular to the modern shoreline, perhaps due to directed coastal erosion.

5. Discussion

A major strength of our automated deep-seated landslide mapping methods is that they work well in both rural and urban parts of our study areas. Although roads, grading, and other human modifications of the landscape do cause some misclassifications, many modifications do not completely erase the topographic signatures of deep-seated landslides. Anthropogenic topographic features often have higher spatial frequencies than deep-seated landslides in our study areas and therefore do not influence spectral power over our characteristic frequency bands. This filtering of unwanted wavelengths from the data works particularly well in Seattle, where nearly every node in the data has been modified by human activity, but our automated methods still classify 87% of the nodes correctly.

Error indices and percentages of correctly classified terrain both provide measures of how well our automatically generated maps match independently compiled, deep-seated landslide maps, but low error indices and high percentages of correctly mapped terrain do not always correlate. For example, we match the highest percentage of nodes, but also have the highest error index in MTC compared to our other study areas. In DMQ, we have the lowest error index, but also the lowest percentage of nodes classified correctly. These discrepancies result from differences in the abundances of deep-seated landslides in our study areas. To illustrate, we rewrite Eq. (6) as

$$E = 1 - \frac{C_{ls}}{A_{ls} + I_{ls}} \tag{7}$$

where C_{ls} is the area of correctly identified landslide nodes, A_{ls} is the total area of mapped landslide nodes, and I_{ls} is the area of incorrectly classified landslide nodes. In our data sets where A_{ls} is a high percentage of the total area (DMQ and NWD), C_{ls} can approach A_{ls} while I_{ls} remains low because very little land area exists to be classified as I_{ls}. On the other hand, when A_{ls} is only a small percentage of the total area (MTC, SEA, and CBP), I_{ls} has the potential to become quite high as C_{ls} approaches A_{ls} simply because a large area of unfailed terrain exists. The former case tends to allow the ratio in Eq. (7) to approach 1, leading to a low E, while the latter case tends to keep the ratio small, leading to a high E. These discrepancies between error index and percentage of correctly classified nodes suggest that close visual inspection of maps may be required in addition to statistical measures to thoroughly evaluate the quality of the match between different landslide inventory maps of the same study area.

Our windowed 2D DFT and 2D CWT algorithms perform comparably to one another in each study area, but the 2D CWT shows more promise in future applications for several reasons. Most importantly, the 2D CWT applied to topographic data preserves information about position in addition to frequency, so it is more suited to visualization of spatial patterns of spectral power. Inspection of a study area's wavelet coefficients and dominant wavelength map allows both node-

by-node analysis of specific morphologic features and investigation of broad spatial patterns. We chose the Mexican hat wavelet for our study because of its resemblance to a landslide hummock, but numerous other families of wavelets exist that may be better suited to different study areas or to extracting different topographic features. Lastly, the choice of wavelet scales is flexible in nonorthogonal wavelet analysis (Torrence and Compo, 1998), so as few or as many scales as needed can be analyzed, depending on the particular application. This differs from orthogonal wavelet analysis, which samples only discrete scale and location parameters (Torrence and Compo, 1998). For the automated mapping presented here, after identifying characteristic wavelengths of deep-seated landslides, we needed only 5 to 7 wavelet scales to map topographic features associated with landslides. This required far less computation time than our windowed Fourier analysis.

Automated landslide mapping methods such as those described here may never completely replace traditional methods of topographic map inspection, aerial photograph interpretation, and fieldwork. In particular, because our automated methods rely entirely upon morphologic expressions as recorded by topographic data, they often do not capture the boundaries between neighboring and overlapping landslides and are insensitive to the details of subsurface geology. However, as high-resolution topographic data become increasingly available, our automated methods will provide effective, objective, and efficient tools that can supplement traditional methods. Our methods quantify and more objectively locate the same topographic features used to map landslides with visual inspection of photographs, maps, or high-resolution data, producing results that can serve as a starting point for a more detailed landslide inventory map in a fraction of the time required for a manual survey.

6. Conclusions

Landslide inventory maps provide valuable information to a variety of policy makers and scientists, but their creation remains a time consuming and subjective task. The increasing availability of high-resolution LiDAR-derived DEMs provides new opportunities for improving the efficiency and objectivity of mapping spatial and temporal patterns of slope instability. However, few studies to date have capitalized on LiDAR-derived DEMs to investigate landsliding at meter-scale resolutions over kilometer-scale swaths of terrain.

We have described two signal processing techniques that can be used to quantify the morphologic expressions of deep-seated landslides using high-resolution topographic data and to map how these expressions vary spatially. Power spectra produced by two-dimensional Fourier and wavelet analyses define the characteristic wavelengths of landslide features in the Puget Sound lowlands, Washington, and the Tualatin Mountains, Oregon. Spectral power summed over a characteristic band of wavelengths provides a measure of the strength of the topographic signature of deep-seated landsliding at any point in a data set. Examining the spectral power sum at each node in mapview highlights patterns of past slope instability over study areas up to hundreds of square kilometers in extent.

To test how well these methods can delineate terrain that has undergone past deep-seated landsliding, we compared the outputs of our algorithms to independently created landslide inventory maps in each study area. We classified the algorithm-generated arrays so as to minimize the error index of the array compared to its corresponding landslide map. Assuming the landslide inventory maps recorded all landslides in each study area, our algorithms were able to match an average of 82% of the area in our five study areas. These results indicate that the 2D DFT and 2D CWT are capable of producing accurate deep-seated landslide maps in our study areas. Although we do not see automated methods replacing traditional landslide mapping methods, we propose that they can improve the objectivity of landslide mapping and decrease the time needed to compile landslide inventory maps.

Lastly, we created a dominant wavelength map to investigate the relationship between geomorphic processes and their topographic expressions. Spatial variations in dominant wavelength within deep-seated landslides highlight how deep-seated landsliding concentrates spectral power over intermediate wavelengths by dissecting the landscape into blocks and by forming hummocks of a particular spatial scale. Diffusive soil transport shifts spectral power to longer dominant wavelengths, while fluvial incision also dissects the surfaces of inactive deep-seated landslides at longer spatial scales. We suggest that dominant wavelength maps may be a useful tool for analyzing the topographic expressions of a suite of geomorphic processes over a wide range of scales.

Acknowledgements

Thank you to H. Kelsey for an insightful review that helped improve the depth of this contribution. This work was supported by an NSF Graduate Research Fellowship to AMB, NSF Award EAR-0447190 to JJR, an R.A. Daly Postdoctoral Fellowship to JTP, and the University of Oregon Department of Geological Sciences.

References

Addison, P.S., 2002. The Illustrated Wavelet Handbook: Introductory Theory and Applications in Science, Engineering, Medicine and Finance. Institute of Physics Publishing, Bristol, UK.

Armstrong, J.E., Crandell, D.R., Easterbrook, D.J., Noble, J.B., 1965. Late Pleistocene stratigraphy and chronology in southwestern British Columbia and northwestern Washington. GSA Bulletin 76, 321–330.

Beeson, M.H., Tolan, T.L., Madin, I.P., 1989. Geologic Map of the Lake Oswego Quadrangle, Clackamas, Multnomah and Washington Counties, Oregon. Geologic Map Series 59, Oregon Department of Geology and Mineral Industries, Portland, OR.

Beeson, M.H., Tolan, T.L., Madin, I.P., 1991. Geologic Map of the Portland Quadrangle, Multnomah and Washington Counties, Oregon. Geologic Map Series 75, Oregon Department of Geology and Mineral Industries, Portland, OR.

Booth, D.B., 1987. Timing and processes of deglaciation along the southern margin of the Cordilleran ice sheet. In: Ruddiman, W.F., WrightJr. Jr., H.E. (Eds.), North America and Adjacent Oceans During the Last Deglaciation; The Geology of North America, K-3. Geological Society of America, Boulder, CO, pp. 71–90.

Carrara, A., Cardinali, M., Guzzetti, F., 1992. Uncertainty in assessing landslide hazard and risk. ITC Journal 2, 172–183.

Chadwick, J., Glenn, N., Thackray, G., Dorsch, S., 2005. Landslide surveillance: new tools for an old problem. Eos 86 (11), 109–114.

Cruden, D.M., Varnes, D.J., 1996. Landslide types and processes. In: Turner, A.K., Schuster, R.L. (Eds.), Landslides Investigation and Mitigation. National Academy Press, Washington, DC, pp. 36–75.

Galli, M., Ardizzone, F., Cardinali, M., Guzzetti, F., Reichenbach, P., 2008. Comparing landslide inventory maps. Geomorphology 94, 268–289. doi:10.1016/j.geomorph.2006.09.023.

Galster, R.W., Laprade, W.T., 1991. Geology of Seattle, Washington, United States of America. Bulletin of the Association of Engineering Geologists 28 (3), 235–302.

Glenn, N.F., Streutker, D.R., Chadwick, D.J., Thackray, G.D., Dorsch, S.J., 2006. Analysis of LiDAR-derived topographic information for characterizing and differentiating landslide morphology and activity. Geomorphology 73, 131–148.

Guzzetti, F., Carrara, A., Cardinali, M., Reichenbach, P., 1999. Landslide hazard evaluation: a review of current techniques and their application in a multi-scale study, Central Italy. Geomorphology 31, 181–216.

Guzzetti, F., Cardinali, M., Reichenbach, P., Carrarra, A., 2000. Comparing landslide maps: a case study in the upper Tiber River basin, central Italy. Environmental Management 25 (3), 247–263. doi:10.1007/s002679910020.

Hanley, J.T., 1977. Fourier analysis of the Catawba Mountain knolls, Roanoke County, Virginia. Mathematical Geology 9 (2), 159–163.

Harrison, J.M., Lo, C.P., 1996. PC-based two-dimensional discrete Fourier transform programs for terrain analysis. Computers and Geosciences 22 (4), 419–424.

Haugerud, R.A., Harding, D.J., Johnson, S.Y., Harless, J.L., Weaver, C.S., Sherrod, B.L., 2003. High resolution Lidar topography of the Puget Lowland, Washington — a bonanza for earth science. GSA Today 13 (6), 9.

Hovius, N., Stark, C.P., Allen, P.A., 1997. Sediment flux from a mountain belt derived by landslide mapping. Geology 25 (3), 231–234.

Hovius, N., Stark, C.P., Hao-Tsu, C., Jiun-Chuan, L., 2000. Supply and removal of sediment in a landslide-dominated mountain belt: Central Range, Taiwan. Journal of Geology 108, 73–89.

Jordan, G., Schott, B., 2005. Application of wavelet analysis to the study of spatial pattern of morphotectonic lineaments in digital terrain models. A case study. Remote Sensing of the Environment 94, 31–38.

Kumar, P., Foufoula-Georgiou, E., 1994. Wavelet analysis in geophysics: an introduction. In: Foufoula-Georgiou, E., Kumar, P. (Eds.), Wavelets in Geophysics. Academic Press, San Diego, CA, pp. 1–44.

Kumar, P., Foufoula-Georgiou, E., 1997. Wavelet analysis for geophysical applications. Reviews of Geophysics 35 (4), 385–412.
Lashermes, B., Foufoula-Georgiou, E., Dietrich, W.E., 2007. Channel network extraction from high resolution topography using wavelets. Geophysical Research Letters 34, L23S04. doi:10.1029/2007GL031140.
Madin, I.P., Niewendorp, C.A., 2008. Preliminary Geologic Map of the Dixie Mountain Quadrangle, Washington, Multnomah and Columbia Counties, Oregon. Open-File Report O-08-07, Oregon Department of Geology and Mineral Industries, Portland, OR.
Malamud, B.D., Turcotte, D.L., 2001. Wavelet analyses of Mars polar topography. Journal of Geophysical Research 106 (8), 17497–17504.
Malamud, B.D., Turcotte, D.L., Guzzetti, F., Reichenbach, P., 2004a. Landslide inventories and their statistical properties. Earth Surface Processes and Landforms 29, 687–711. doi:10.1002/esp.1064.
Malamud, B.D., Turcotte, D.L., Guzzetti, F., Reichenbach, P., 2004b. Landslides, earthquakes, and erosion. Earth and Planetary Science Letters 229, 45–59.
McKean, J., Roering, J., 2004. Objective landslide detection and surface morphology mapping using high-resolution airborne laser altimetry. Geomorphology 57, 331–351.
McKean, J.A., Isaak, D.J., Wright, C.W., 2008. Geomorphic controls on salmon nesting patterns described by a new, narrow-beam terrestrial-aquatic lidar. Frontiers in Ecology and the Environment 6. doi:10.1890/070109.
Nilsen, T.H., Brabb, E.E., 1977. Slope stability studies in the San Francisco Bay region, California. Geological Society of America, Reviews in Engineering Geology 3, 235–243.
Nilsen, T.H., Wright, F.H., Vlasic, C., Spangle, W.E., 1979. Relative slope stability and land-use planning in the San Francisco Bay region, California. U.S. Geological Survey Professional Paper 944. 104 pp.
Percival, D.P., 1995. On estimation of the wavelet variance. Biometrika 82, 619–631.
Perron, J.T., Kirchner, J.W., Dietrich, W.E., 2008. Spectral signatures of characteristic spatial scales and nonfractal structure in landscapes. Journal of Geophysical Research 113, F04003. doi:10.1029/2007JF000866.
Priestley, M.B., 1981. Spectral Analysis and Time Series. Academic Press, New York.
Rayner, J.N., 1972. The application of harmonic and spectral analysis to the study of terrain. In: Chorley, R.J. (Ed.), Spatial Analysis in Geomorphology. Methuen, London, pp. 283–302.
Roering, J.J., Kirchner, J.W., Dietrich, W.E., 2005. Characterizing structural and lithologic controls on deep-seated landsliding: implications for topographic relief and landscape evolution in the Oregon Coast Range, USA. GSA Bulletin 117, 654–668. doi:10.1130/B25567.1.
Schulz, W.H., 2004. Landslides Mapped Using LIDAR Imagery, Seattle, Washington. Open-File Report 2004-1396, U.S. Geological Survey, Reston, VA, 11 pp, 1 plate.
Schulz, W.H., 2005. Landslide Susceptibility Estimated from Mapping Using Light Detection and Ranging (LIDAR) Imagery and Historical Landslide Records, Seattle, Washington. Open-File Report 2005-1405, U.S. Geological Survey, Reston, VA, 16 pp, 1 plate.
Schulz, W.H., 2007. Landslide susceptibility revealed by LIDAR imagery and historical records, Seattle, Washington. Engineering Geology 89, 67–87.
Slatton, K.C., Carter, W.E., Shrestha, R.L., Dietrich, W., 2007. Airborne laser swath mapping: achieving the resolution and accuracy required for geosurficial research. Geophysical Research Letters 34, L23S10. doi:10.1029/2007GL031939.
Torrence, C., Compo, G.P., 1998. A practical guide to wavelet analysis. Bulletin of the American Meteorological Society 79 (1), 61–78.
Trimble, D.E., 1963. Geology of Portland, Oregon and adjacent areas. Bulletin 1119, U.S. Geological Survey, Washington, DC, 119 pp.
Tubbs, D.W., 1974. Landslides in Seattle. Washington Division of Geology and Earth Resources Information Circular 52, 15 pp., 1 plate.
Tubbs, D.W., 1975. Causes, mechanisms and prediction of landsliding in Seattle. Seattle, University of Washington, Ph.D. dissertation, 89 pp., 1 plate.
Van Den Eeckhaut, M., Poesen, J., Verstraeten, G., Vanacker, V., Moeyersons, J., Nyssen, J., van Beek, L.P.H., 2005. The effectiveness of hillshade maps and expert knowledge in mapping old deep-seated landslides. Geomorphology 67, 351–363.
Van Den Eeckhaut, M., Poesen, J., Verstraeten, G., Vanacker, V., Nyssen, J., Moeyersons, J., van Beek, L.P.H., Vandekerckhove, L., 2007a. Use of LIDAR-derived images for mapping old landslides under forest. Earth Surface Processes and Landforms 32, 754–769.
Van Den Eeckhaut, M., Verstraeten, G., Poesen, J., 2007b. Morphology and internal structure of a dormant landslide in a hilly area: the Collinabos landslide (Belgium). Geomorphology 89, 258–273.
Wieczorek, G.F., 1984. Preparing a detailed landslide-inventory map for hazard evaluation and reduction. Bulletin of the Association of Engineering Geologists 21 (3), 337–342.
Wills, C.J., McCrink, T.P., 2002. Comparing landslide inventories, the map depends on the method. Environmental and Engineering Geoscience 8, 279–293.

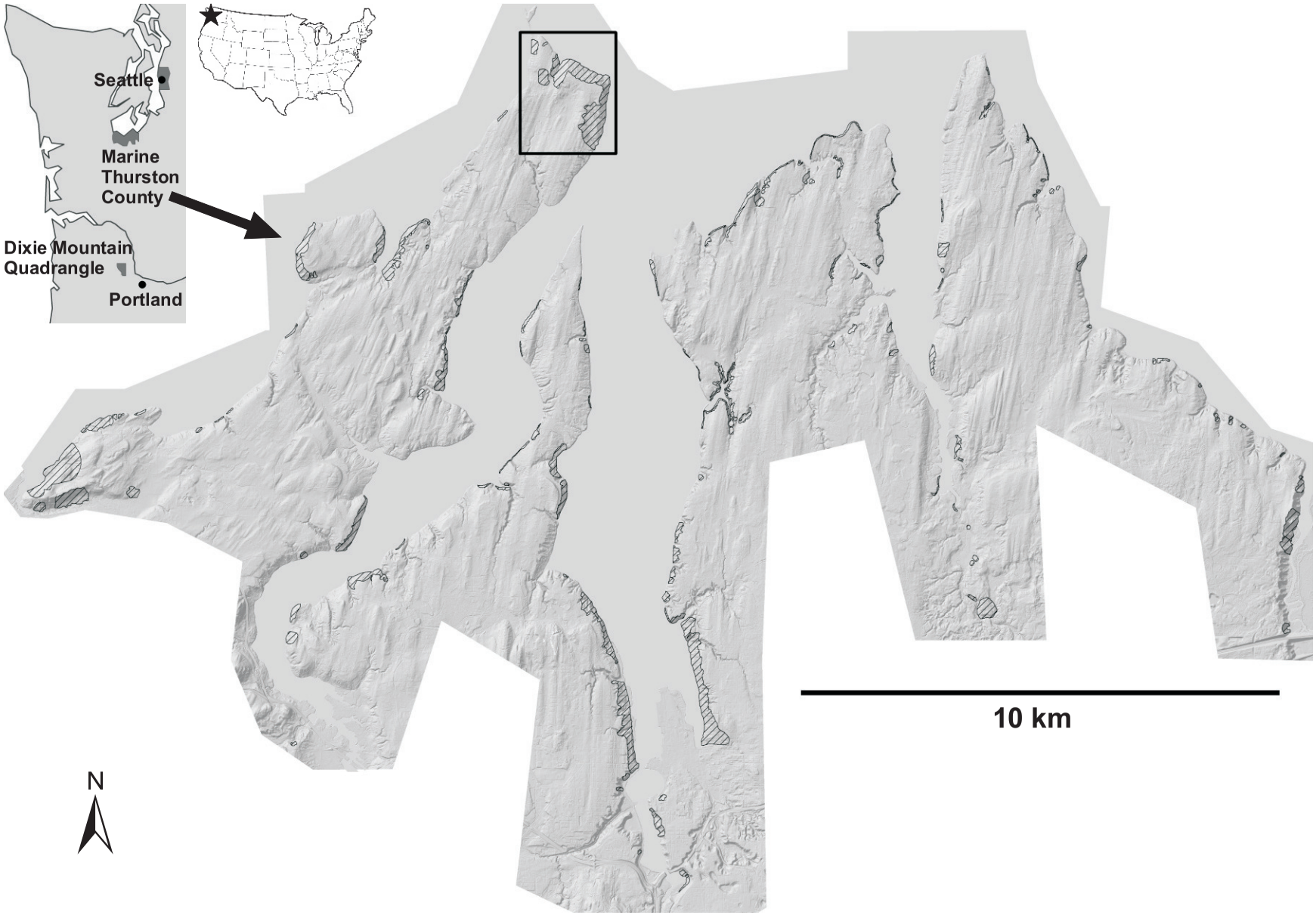
Seattle
Marine
Thurston
County
Dixie Mountain
Quadrangle
Portland
10 km
N

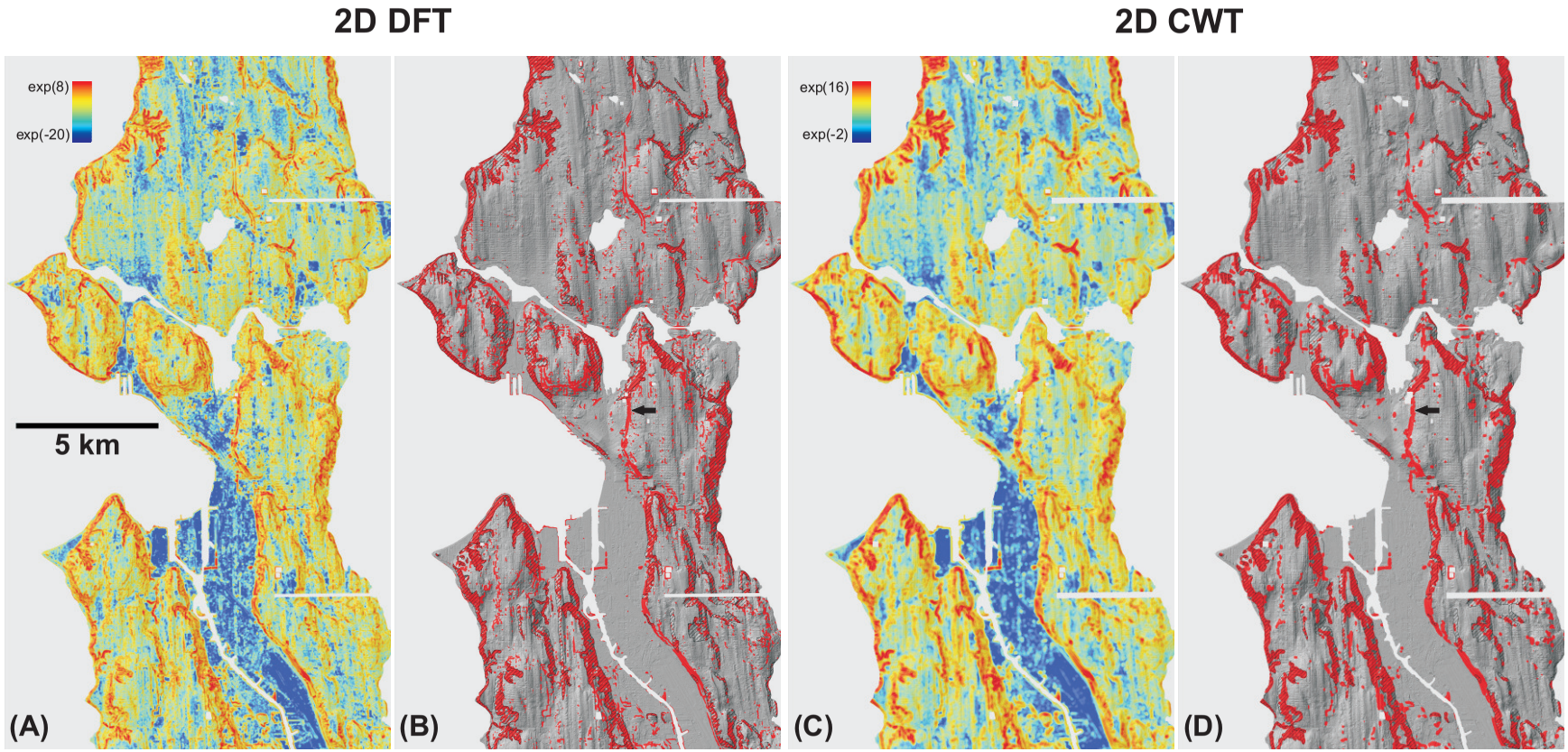
2D DFT
2D CWT
exp(8)
exp(-20)
exp(16)
exp(-2)
5 km
(A)
(B)
(C)
(D)